IPEM
Institute of Physics and
Engineering in Medicine

Performance evaluation of the ECAT HRRT: an LSO-LYSO double layer high resolution, high sensitivity scanner

View the article online for updates and enhancements.

Performance evaluation of the ECAT HRRT: an LSO-LYSO double layer high resolution, high sensitivity scanner

Hugo W A M de Jong, Floris H P van Velden, Reina W Kloet, Fred L Buijs, Ronald Boellaard and Adriaan A Lammertsma

Department of Nuclear Medicine & PET Research, VU University Medical Centre, Amsterdam, The Netherlands

E-mail: h.w.a.m.dejong@umcutrecht.nl

Abstract

The ECAT high resolution research tomograph (HRRT) is a dedicated brain and small animal PET scanner, with design features that enable high image spatial resolution combined with high sensitivity. The HRRT is the first commercially available scanner that utilizes a double layer of LSO/LYSO crystals to achieve photon detection with depth-of-interaction information. In this study, the performance of the commercial LSO/LYSO HRRT was characterized, using the NEMA protocol as a guideline. Besides measurement of spatial resolution, energy resolution, sensitivity, scatter fraction, count rate performance, correction for attenuation and scatter, hot spot recovery and image quality, a clinical evaluation was performed by means of a HR+/HRRT human brain comparison study. Point source resolution varied across the field of view from approximately 2.3 to 3.2 mm (FWHM) in the transaxial direction and from 2.5 to 3.4 mm in the axial direction. Absolute line-source sensitivity ranged from 2.5 to 3.3% and the NEMA-2001 scatter fraction equalled 45%. Maximum NECR was 45 kcps and 148 kcps according to the NEMA-2001 and 1994 protocols, respectively. Attenuation and scatter correction led to a volume uniformity of 6.3% and a system uniformity of 3.1%. Reconstructed values deviated up to 15 and 8% in regions with high and low densities, respectively, which can possibly be assigned to inaccuracies in scatter estimation. Hot spot recovery ranged from 60 to 94% for spheres with diameters of 1 to 2.2 cm. A high quantitative agreement was met between HR+ and HRRT clinical data. In conclusion, the ECAT HRRT has excellent resolution and sensitivity properties, which is a crucial advantage in many research studies.

(Some figures in this article are in colour only in the electronic version)

1. Introduction

In the last decade PET has been recognized as an indispensable instrument in measuring molecular pathways and interactions *in vivo*, both in clinical diagnostics and in clinical and pre-clinical research. PET can be used to study processes such as metabolism, tissue perfusion or receptor occupancy, making it a valuable tool in studying the functioning of complex organs including the human brain (Lammertsma 2001, Wang and Maurer 2005).

Recently, interest has arisen to study these processes in small laboratory animals. This is a result not only from the ongoing restrictions on the use of large quantities of research animals, but also coincides with the increasing availability of animal models of several diseases (Lammertsma *et al* 1995, Pomper and Lee 2005).

PET research of both human brain and small animals demands scanners featuring high image resolution. A prerequisite for actually achieving high spatial resolution is high sensitivity over a large range of activities (Lammertsma *et al* 1995)[1].

Altogether, this has encouraged the development of dedicated research scanners (Beekman *et al* 2005, Chatziioannou *et al* 1999, Cherry *et al* 1997, Schramm *et al* 2003, Tsuda *et al* 2006, Weber *et al* 1999). Coincidently, new developments in crystal technologies such as the availability of LSO and the improvement of crystal cutting techniques have enabled the manufacturing of smaller crystal element sizes combined with higher photon counting rates (Casey *et al* 1997, Schmand *et al* 1998). Together with the advances in electronic signal processing, this has paved the way for the production of scanners with limited dead time effects. The required high sensitivity can be achieved by using thicker crystals combined with the omission of septa (3D PET). Unfortunately, the use of thicker crystals tends only to degrade the resolution, especially at the edge of the field of view (FOV). To oppose this so-called parallax effect, a technique known as phoswich to measure the depth of interaction (DOI) has been proposed (Bartzakos and Thompson 1991, Seidel *et al* 2003).

The ECAT high resolution research tomograph (HRRT, CTI/Siemens) combines all the above-mentioned technological innovations including DOI by means of two crystal layers. The scanner was especially designed for human brain and small animal research. The purpose of this study was to fully characterize the performance of the HRRT.

Development of the HRRT started in the late 1990s with the production of two prototypes. The double layer prototype HRRT consisted of five detector heads with two 7.5 mm thick LSO layers and three detector heads with an LSO layer and a GSO layer, both 7.5 mm thick (Heiss *et al* 2004, Wienhard *et al* 2002), whereas the single layer prototype had only one layer of LSO crystals (Boellaard *et al* 2003a). Apart from the crystals used, both scanners were technically equivalent. The performance of both prototypes has been published before.

Several years later, based on the practical experiences with these prototypes a commercial version of the HRRT was taken into production. This HRRT consisted of an LSO and an LYSO crystal layer, each 10 mm thick. Furthermore, significant improvements were made to its electronics design, to its transmission system and in the area of the data acquisition hardware and reconstruction methods.

The many technical innovations used in the scanner and the leading role it is expected to play in future PET brain research justifies publication of the performance of the commercial HRRT. Although specific elements of the performance of mainly the prototype HRRTs have been reported previously (Boellaard *et al* 2003a, 2003b, Eriksson *et al* 2002, 2005, Wienhard *et al* 2002), no study has yet described the complete performance of the commercial HRRT. In order to make sure that all aspects in the scanner performance are included and to make a

---

[1] High resolution images are represented by large image matrices. In order to maintain the image element noise at a doubling matrix size, sensitivity has to be increased eight fold.

comparison with other scanners possible, the standardized NEMA protocols were taken as a basis.

2. Methods

Performance measurements and data analysis were performed according to the procedures published in the NEMA report NU 2-2001 (NEMA-2001) (National Manufacturers Association 2001). This report describes a series of phantom experiments to determine imaging characteristics, including spatial resolution, scatter fraction, count rates, sensitivity, accuracy of correction methods and general image quality. These experiments were, however, designed with a primary focus on whole body imaging for oncological applications. As such, these measurements may not accurately represent the performance of a PET scanner for brain imaging applications. Therefore, in addition to the NEMA-2001 tests, a part of the count rate and scatter fraction tests, together with an assessment of the accuracy of subsequent corrections, performed with the original NEMA report NU 2-1994 (NEMA-1994) phantom was also included (National Manufacturers Association 1994). This smaller phantom tends to better predict the performance of a brain study. For the same reason, the NEMA-2001 thorax-shape image quality phantom was replaced by an anthropomorphic brain phantom and a cylinder phantom with hot and cold spots, as suggested by Daube-Witherspoon et al (2002). Finally, some example images of applications in human brain and small animal research are given.

3. Scanner description

In contrast to the detector rings used in the majority of PET scanners, the HRRT consists of eight panel detectors (detector heads), which are arranged in an octagon to allow for the use of quadrant sharing (Wong et al 1995); a detector head contains 117 detector blocks arranged in a 9×13 array which are read out by a 10×14 array of photomultiplier tubes (PMTs). Each detector block ($19 \times 19 \times 20$ mm^3) is cut into 8×8 crystal elements. Although the crystals are only 2.1×2.1 mm^2, the quadrant sharing assures a good crystal separation in the photon detection position. Each block consists of a 10 mm LSO and a 10 mm LYSO crystal layer. DOI information can be retrieved by measuring the crystal light decay time, which is slightly faster for LSO (40 ns) as compared to LYSO (53 ns). Coincidence timing window is set at 6 ns. The scanner FOV is 312 mm in diameter and 250 mm in axial length, which allows for human whole-brain studies and scans of rodents and primates (figure 1).

Although the set-up of the scanner, which includes adjustment of the PMT gains, CFD (constant fraction discrimination) settings, mutual time alignment, definition of crystal region maps and the 511 keV peaks of the detector blocks, is automated, in practice it requires significant manual fine tuning and is therefore time consuming.

By default, the acquired data are stored in a list with 64 bits per coincidence event (prompt or random), referred to as a 64 bits list mode. At every millisecond, a time tag is added to the list. For reconstruction, the list mode data are binned into (time series of) prompts minus delays (trues plus scatters) or separate randoms and prompts sinograms. The standard compression used is span 9, resulting in 256 radial bins, 288 angles and 2209 planes, of which 207 are non-oblique. Span 3 sinograms are also supported, but are excessively large in size (1 Gbyte per frame) making data handling and reconstruction challenging for most computer systems. Randoms are estimated by means of a delayed window technique. In order to correct the sinograms for (geometric) inhomogeneities and variations in detector

Figure 1. Left: commercial HRRT. Right: example of a set-up for multi small animal scanning.

sensitivities, normalization data need to be acquired using a rotating line source. For transmission measurements, a 740 MBq 2D fan-collimated Cs-137 (single photon emitter) moving point source is used. For reconstruction of the transmission data, several iterative algorithms are available including NEC-TR (Nuyts *et al* 2001) and a map-TR algorithm, the latter taking *a priori* information about the density of expected material (water, air, tissue) into account (De Jong *et al* 2004). Scatter correction is performed using an adapted version of the single scatter simulation method of Watson (2000). Finally, dead time correction is based on an empirical relation between the detected singles rate and the trues rate dead time (De Jong *et al* 2005b).

Supported image reconstruction methods are 2D FPB, 2D OSEM (both using Fourier rebinning (Defrise *et al* 1997)) and 3D OSEM. The latter algorithm is the method preferred by most users, since it produces the highest quality images in terms of signal to noise. Furthermore, the existence of gaps in HRRT sinograms complicates the use of 2D reconstruction algorithms (De Jong *et al* 2003).

Because 3D OSEM is a time-consuming reconstruction algorithm, especially in the case of the large sinogram sizes generated by the HRRT, the manufacturer supports a 16 node computer cluster (Vollmar *et al* 2002). Furthermore, several 3D OSEM variants can be used, of which the OP-OSEM (ordinary Poisson) is currently the method of choice, due to its capability to limit image bias at low count statistics (Comtat *et al* 2004).

In conclusion, although the user has many options to his disposal, the standard acquisition and reconstruction methods on which the tests in this study were based are lower and upper energy window settings of 400 and 650 keV, acquisition in a 64 bits list mode, sinogram size in span 9 and reconstruction of transmission maps using the NEC-TR algorithm and emission data using 3D OP-OSEM (8 iterations and 16 subsets). All images were reconstructed with a matrix of $256 \times 256 \times 207$ and a pixel size of $1.218 \times 1.218 \times 1.218$ mm^3.

The L(Y)SO crystals used in the HRRT contain a small fraction of ^{176}Lu. This intrinsic radioactivity is known to generate background radiation causing randoms in turn, as well as a small fraction of true coincidences due to cascading gamma rays. Although this background is low enough to have no significant influence on the acquired data in clinical practice (on average less than 1×10^{-5} counts per second (cps) per LOR), it can have a slight influence on scanner characteristics, especially when measured at very low activity levels. To counter this, Watson *et al* (2004) suggested slight alterations to the NEMA protocol. To this end a characteristic extrinsic activity threshold (a_{ref}) is defined above which the response of the

scanner is determined more by the radiation originating external to the detectors than by the internal activity (Watson *et al* 2004). For the HRRT, an a_{ref} of 5 MBq in a 70 cm phantom was found. This activity threshold was used to define the used activities for the resolution and the sensitivity measurements.

4. Performance measurement

4.1. Spatial resolution

To determine the resolution of the scanner, a point source with an initial ^{18}F activity of 2 MBq was prepared as required: a glass capillary with an inner diameter of 1 mm and an outer diameter of 2 mm was filled with a droplet of activity with a length of 1 mm. According to NEMA-1994, the source was positioned in the axial central plane and parallel to the tomographical axis and measured in air at radial distances of 0, 1, 5, 10 and 14 cm with a minimum of 10^5 counts for every position. Furthermore, additional point source locations were chosen as described in NEMA-2001. Although both NEMA protocols prescribe only the use of (2D) FBP for this measurement, the images were also reconstructed with 3D OP-OSEM to comply with clinical practice.

The OSEM algorithm is, however, known to overestimate the resolution of point sources in air. Therefore, in addition to the point source reconstructions a series of acquisitions of a hot line source (inner diameter 1 mm, length 60 mm) placed in a warm cylinder (diameter 30 mm, length 60 mm) was performed. The total activity in the line source plus cylinder was again approximately 2 MBq, while the line source to background ratio was circa 15:1. The line source was measured at the locations as prescribed by the NEMA-2001 protocol, placed axially for the tangential and radial resolution and in plane for axial resolution. After reconstruction with 3D OP-OSEM and 2D FBP, resolutions were determined taking the background of the warm cylinder into account.

All sinogram data were corrected for randoms. Furthermore, the used activity is in concordance with the recommendations made by Watson *et al* stating that an activity should be smaller than two times the characteristic extrinsic activity a_{ref} in order to prevent pulse pile-up influencing the widths of the point or line source.

4.2. Scatter fraction, count losses and random measurements

The 70 cm long, 20 cm diameter solid NEMA-2001 phantom with a line source placed off-centre is especially designed to include the effects of the activity located outside the FOV. The phantom is made of polyethylene with a density of 0.96 g cm^{-3}. At a radius of 4.5 cm, a hole is drilled with a diameter of 6.4 mm parallel to the phantom's axis in which a tube containing the activity is inserted. For the count rate measurement, the starting activity was 650 MBq of ^{18}F, which, as the activity would be distributed uniformly over the phantom, can be regarded as a concentration of 29.5 kBq cc^{-1}. Data were acquired during 20 h, or over ten decay times, and histogrammed into a series of 40 frames of 30 min each. For every frame, the prompts rate (cps) and randoms rate (cps) were determined. Scatter fraction was calculated by integrating the number of scattered counts inside and outside a 40 mm strip, as described by the protocol. This protocol also prescribes that for the scatter fraction data shall be used with randoms rate at less than 1.0% of the trues rate. This, however, could not be realized due to the natural activity of LSO (Eriksson *et al* 2005, Huber *et al* 2002, Vaska and Alexoff 2003). Therefore, in accordance with the suggestion of Watson *et al* (Brambilla *et al* 2005, Watson *et al* 2004), the scatter fraction as a function of activity in the FOV was measured using prompts minus

delays sinograms. Furthermore, the data were corrected for the intrinsic background. Whole gantry and slice-by-slice scatter fractions were reported for 2.5 kBq cc^{-1}.

The scatter fraction was also measured according to NEMA-1994 that prescribes a 20 cm diameter, 20 cm long phantom inserted with a line source that is measured at three positions. The NEMA-1994 scatter fraction, however, was only measured at a low activity of 2.5 kBq cc^{-1}.

Using these scatter fractions and the detected prompts and randoms rate in an area of 240 mm around the line source, the NEC-2R rate could be calculated. For the NEMA-1994 count rate experiment, the same phantom is uniformly filled with a start activity of 43.3 kBq cc^{-1} of ^{18}F. Data analysis was similar to the NEMA-2001 data, except for the scatter fraction, which was based on a weighed average of the three line-source measurements.

4.3. Sensitivity

As defined in NEMA-2001, the sensitivity of a PET scanner is expressed in counts per second per becquerel (cps Bq^{-1}) and measured as suggested by Bailey *et al* (1991). The use of a range of aluminium sleeves enables measuring the absolute sensitivity without the influence of photon attenuation, but with enough material surrounding the source to ensure annihilation of the positrons. The phantom consists of a line source of 3 mm inner diameter and a length of 75 cm. It was filled with 2.87 MBq of ^{18}F, resulting in dead time losses of less than 2% and aligned with the centre of the transaxial field of view. The recommendations made by Watson *et al* concerning the natural background of L(Y)SO are met by keeping the activity below the extrinsic activity a_{ref} and correcting the data for the intrinsic trues and randoms. Emission data were acquired during 300 s. Five aluminium sleeves (length 70 cm) with increasing inner diameter and a constant wall thickness of 0.95 mm were added to the line source, and the acquisition was repeated for each additional sleeve. Decay, randoms and intrinsic trues-corrected count rates were plotted against cumulative aluminium thickness on a logarithmic scale. The absolute sensitivity was then obtained by extrapolating the data to zero thickness using linear regression. Similar to the scatter fraction experiment, randoms subtraction was used prior to data analysis. A sensitivity profile was plotted by analysing the data plane by plane. To obtain absolute scanner sensitivity, the sensitivity obtained was corrected for the natural abundance of positron decay in ^{18}F and the fraction of the line source in the field of view.

Volume sensitivity was determined according to NEMA-1994. To this end, the total counts within the central 17.0 cm of the axial field of view from a uniform 20 cm diameter, 20 cm length phantom were measured and corrected for acquisition time, activity in the phantom and scatter fraction, and compared to the activity concentration as measured in a dose calibrator.

4.4. Accuracy of corrections for count losses and randoms

In order to assess the linearity of the scanner, data acquired for the count rate experiment described in section 5.2 were used. After the activity was completely decayed, a transmission scan was acquired using the scanning ^{137}Cs point source, an energy window setting of 600–800 keV and a total scan time of 6 min. The transmission data were reconstructed using the NEC-TR algorithm. The NEMA protocols prescribe that for assessing the scanner linearity, reconstructed data are to be corrected for randoms, dead time, attenuation and scatter and compared to reconstructions acquired at a randoms rate below 1.0% of the trues rate. Since the natural activity of LSO prevents this, the reconstructed image values were compared with the image at the lowest random/prompt ratio. All data were reconstructed with 2D FBP and

3D OP-OSEM, including all corrections. The relative count rate error (per slice) was plotted for both the NEMA-1994 and the NEMA-2001 data sets.

4.5. Image quality, accuracy of attenuation and scatter corrections

NEMA-2001 prescribes the use of a thorax-shaped phantom equipped with a central cylinder with lower density to mimic lungs and hot and cold spheres. Because this phantom is not very suitable to assess a brain scanner, it was replaced by the anthropomorphic Hoffman brain phantom (Data Spectrum Corporation, USA) and a cylinder filled with hot and cold spheres. In this latter phantom, the two largest spheres (25 and 31 mm diameter) were filled with water for cold lesion imaging, while the background compartment was filled with 6 kBq cc^{-1} of ^{18}F. The four smallest spheres (10 mm, 13 mm, 17 mm and 22 mm) were filled with 48 kBq cc^{-1} and 24 kBq cc^{-1}, to achieve hot spot to background ratios of 8:1 and 4:1, respectively. In order to simulate a clinical situation, the Hoffman phantom was filled with ^{18}F activity concentration of 7 kBq cc^{-1}. Furthermore, in order to assess the accuracies of attenuation and scatter correction, the NEMA-1994 non-uniform cylinder phantom with cylindrical water, air and Teflon inserts, was added to this set. The starting background activity in this phantom was 25 kBq cc^{-1}.

All phantoms were acquired for 15 min whereafter span 9 sinograms were reconstructed with 3D OP-OSEM including all corrections. Transmission acquisitions were only started after ten half-lives of ^{18}F. In accordance with the guidelines, circular 30 mm regions of interest (ROIs) were placed in the background and on the inserts of the reconstructed non-uniform NEMA-1994 phantom for image analysis. The reconstructed average activity and the sphere volumes of the hot and cold spot phantom were calculated using a circular ROI with a diameter equal to the sphere diameter. For every sphere size, 60 background ROIs were drawn throughout the phantom.

4.6. Examples of human brain and small animal scans

For an example of human brain imaging performance, a volunteer was injected with 370 MBq of [^{18}F]-FP-ß-CIT. First the volunteer was imaged on the ECAT HR+, which has a reconstructed resolution (hence after post-filtering) of about 7 mm (Brix *et al* 1997), using a dynamic acquisition protocol. In accordance with the clinical protocol, the acquisition duration was 90 min to enable modelling of the slow irreversible kinetics of the tracer. Following this scan, the patient was transferred to the HRRT scanner and an additional scan of 15 min was acquired, starting approximately 120 min post-injection. After alignment of HRRT with HR+ images, time-activity curves of the striatum, cerebellum and white matter were generated from both data sets. Finally, an example of an FDG rat scan was included to illustrate the capabilities of the scanner to image not only the human brain in high resolution, but also small laboratory animals.

5. Results

5.1. Spatial resolution

Table 1 shows the resolutions in mm measured at the locations prescribed by NEMA-2001 reconstructed with 2D FBP and 3D OP-OSEM. For all locations, in-plane resolution proved very uniform ranging between 2.3 mm in the centre of the FOV and just over 3.2 mm towards the edge. The higher resolution at 10 cm off-axis is due to the parallax effect, which is still partly present despite the DOI measurement. In the 2D FBP case, the axial blurring was

Table 1. Spatial resolution in three directions for different lateral locations according to the NEMA-2001 protocol. The positions X and Y refer to the in-plane horizontal and vertical positions respectively, Z is the axial position, all measured from the centre of the FOV. The resolutions in brackets are based on measurements of the line source in a warm background.

Position in FOV (cm) (X, Y, Z)	3D OP-OSEM resolution FHWM (mm)			2D FBP resolution FHWM (mm)		
	Radial	Tangential	Axial	Radial	Tangential	Axial
(0, 1, 0)	2.3 (2.6)	2.3 (2.5)	2.5 (2.5)	2.6 (2.9)	2.7 (2.7)	3.0 (2.9)
(0, 10, 0)	2.6 (2.6)	3.2 (2.8)	3.4 (2.9)	3.0 (3.3)	3.1 (2.9)	5.7 (5.5)
(10, 0, 0)	3.2 (3.1)	2.7 (2.6)	3.4 (2.8)	3.0 (3.2)	3.1 (3.0)	5.1 (5.1)
(0, 1, 6)	2.4 (2.3)	2.3 (2.5)	2.5 (2.4)	2.5 (2.7)	2.9 (2.7)	2.9 (3.5)
(0, 10, 6)	2.6 (2.8)	3.2 (2.7)	3.4 (3.4)	2.9 (3.1)	3.0 (3.0)	5.4 (5.0)
(10, 0, 6)	3.2 (3.0)	2.5 (2.7)	3.3 (3.1)	3.0 (3.0)	3.2 (2.7)	5.3 (5.4)

significant, an effect that was less present in the 3D OSEM images. This is a known effect of the Fourier rebinning algorithm (see, e.g., Matej *et al* (1998)). Also included are resolutions based on the line source in a warm background, which give sometimes a better representation of the actual image resolution, especially when using an iterative algorithm (table 1). Although these line-source resolutions are in general agreement with the results from the point sources in air, more fluctuations are present in this data. These might be introduced by small inaccuracies in background estimation at the level of the line source due to noise and non-uniformities. Furthermore, small misalignments of the line source with the image matrix can have more degrading consequences than in the case of using small point sources.
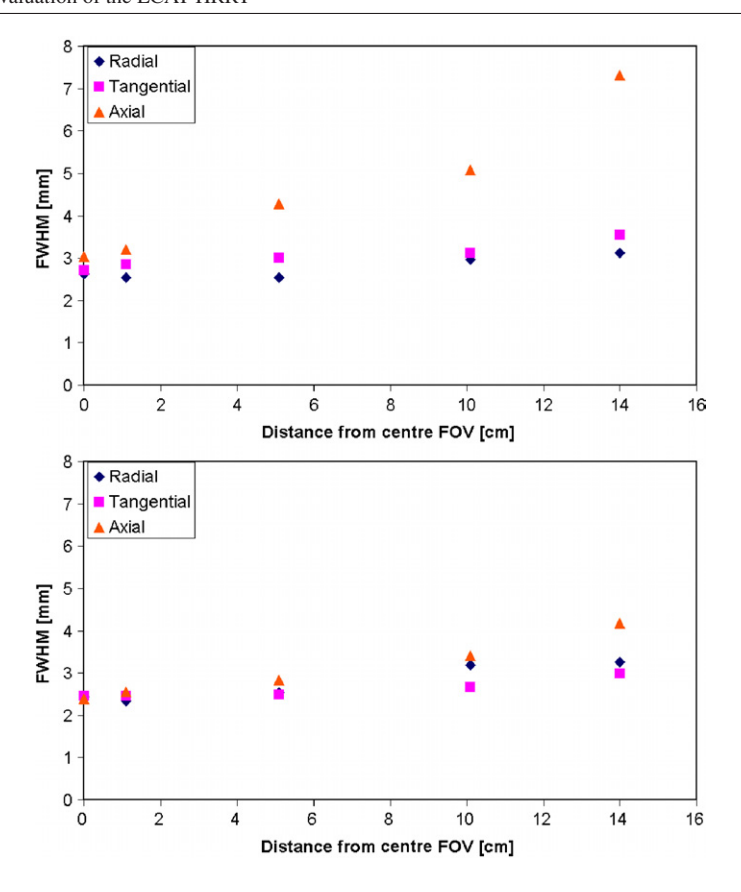
Figure 2 shows the resolution in FWHM of the different point source locations in air according to NEMA-1994. As compared to 2D FBP, the 3D OP-OSEM resolution is approximately 20% better in the image plane (radial and tangential resolutions), while the axial 2D FPB resolution is almost two times lower than the 3D OP-OSEM numbers. In general, the 3D OP-OSEM resolution is fairly constant throughout the FOV (within 20%).

5.2. Scatter fraction, count losses and random measurements

The scatter fraction and prompts and randoms count rates were measured with the NEMA-1994 20 cm length, 20 cm diameter cylinder and the NEMA-2001 70 cm length, 20 cm diameter cylinder. For SFs the 20 cm cylinder was equipped with a line source measured at three different positions (0, 4.5 and 9 cm off-centre), while for the 70 cm cylinder only a line source was placed at 4.5 cm off-centre. Using an identical processing scheme, the number of unscattered and scattered trues was measured in the line-source sinograms for every plane. Prior to this, the sinogram data were corrected for randoms and intrinsic trues.

In order to investigate potential count rate dependence, the NEMA-2001 SF is plotted as a function of activity in the FOV in figure 3. Clearly, the SF increases slightly with increasing activity in the FOV, possibly due to pulse pile-up.

Figure 3 also shows the scatter fractions from plane 30 to 170, which is the central 17 cm of the FOV. The NEMA-1994 scatter fraction shows a dependence on the axial position in the cylinder and is overall lower as compared to the NEMA-2001 scatter fraction. This is probably due to the longer phantom generating more out-of-field scatter and the fact that this scatter fraction is based on just one line-source measurement, which cause it to be slightly overestimated (Daube-Witherspoon *et al* 2002). Whole gantry scatter fractions are given in table 2.
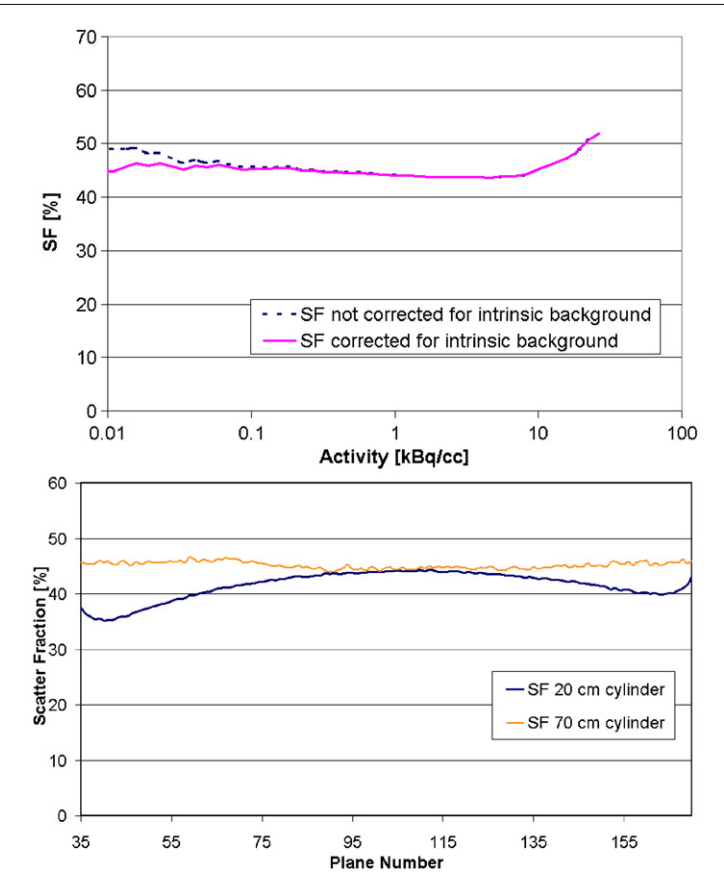
Figure 2. Spatial resolution in three directions for different lateral locations in the FOV. Resolutions are based on point sources measured in air and reconstructed with 2D FBP (top) or 3D OSEM (bottom).

Table 2. Whole FOV (central 17 cm) scatter fraction measured per plane using the 20 cm (NEMA-1994) and the 70 cm (NEMA-2001) cylinders.

20 cm cylinder	70 cm cylinder
41.6%	45.2%

Figure 4 shows the count rate curves as a function of the activity concentration in the total cylinder for the NEMA-1994 and the NEMA-2001 phantoms. Using the smaller phantom, a maximum was reached at approximately 30 kBq cc^{-1}. The NEMA-2001 count rate curve has a similar maximum, but this is reached at a lower activity concentration due to the higher fraction of FOV the cylinder occupies (an equivalent activity concentration corresponds to a higher total activity in the FOV) and because the out-of-FOV activity adds to the randoms and thus total prompts rate. For activity concentrations lower than 22 and 12 kBq cc^{-1}, the correction for decay and dead time results in dose-independent trues rate for both phantoms. This indicates an accurate estimate of the scanner dead time. The decay correction factor was arbitrarily set to 1 at the highest activity level; hence, the resulting corrected trues rate in cps is also arbitrary. In practice, calibration experiments are to be performed to enable conversion from cps to Bq cc^{-1}.

Figure 3. Top: NEMA 2001 scatter fraction as a function of activity in the FOV. Bottom: plane-by-plane scatter fraction measured using the 20 cm (NEMA-1994) and the 70 cm (NEMA-2001) cylinders.

As can be seen in figure 5 (top) the drop at higher activity levels (above 28 kBq cc^{-1}) was not present in the gantry count rates and, hence, could be attributed to limitations of the acquisition computer. Overall, the gantry count rate is higher as compared to the sinogram count rates. This is due to the loss of counts when the list mode data are converted to sinogram, thereby omitting line of responses that are outside the maximum ring difference of 67.

Figure 5 also shows the NEMA-1994 and NEMA-2001 NEC-2R rates. Peak NEC rates are 148 kcps (NEMA-1994) and 45 kcps (NEMA-2001). The lower NEMA-2001 NEC rate maximum is due to the scatter and randoms from activity out of the FOV.

5.3. Sensitivity

Following NEMA-2001 the absolute scanner sensitivity was determined using Bailey's method (Bailey *et al* 1991). Figure 6 gives the slice-sensitivity profiles for the centre and off-centre positions. The plateau between planes 70 and 140 is due to the introduction of a maximum ring difference during sinogram binning. Whole gantry absolute sensitivities are given in table 3. In order to get a true absolute sensitivity, only the activity located in the FOV was taken into account, as suggested by Daube-Witherspoon *et al* (2002). Also included are the
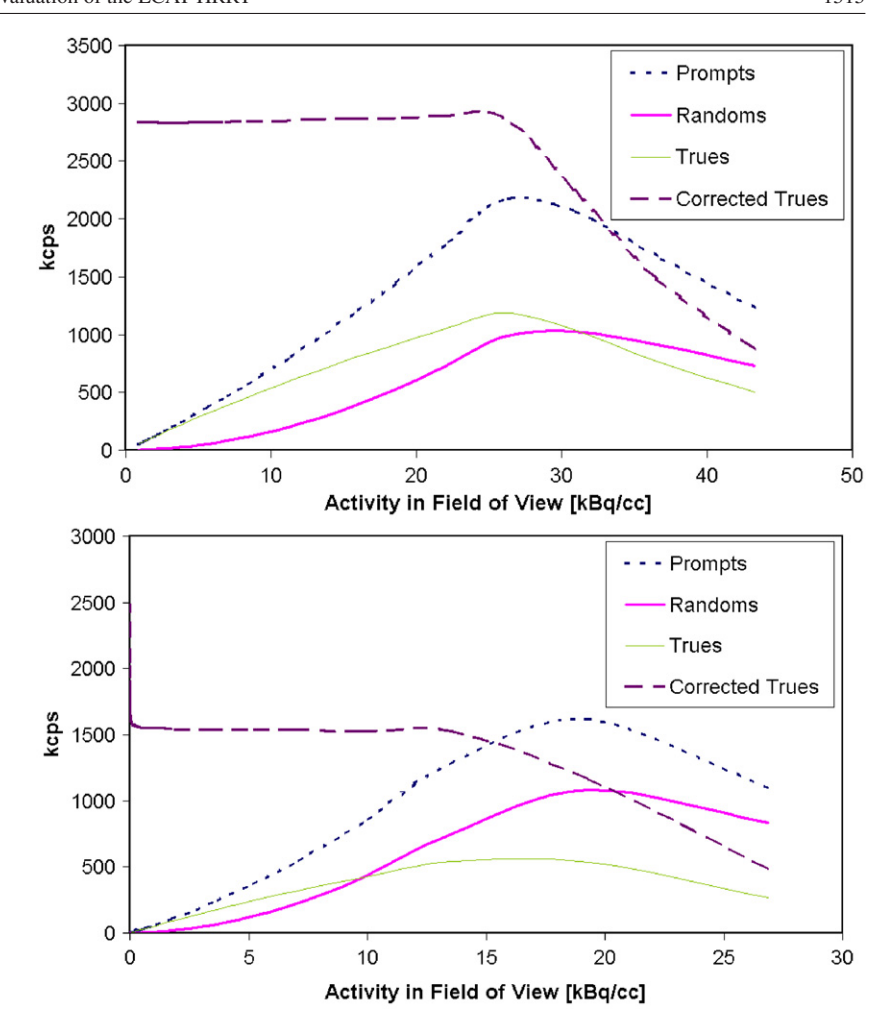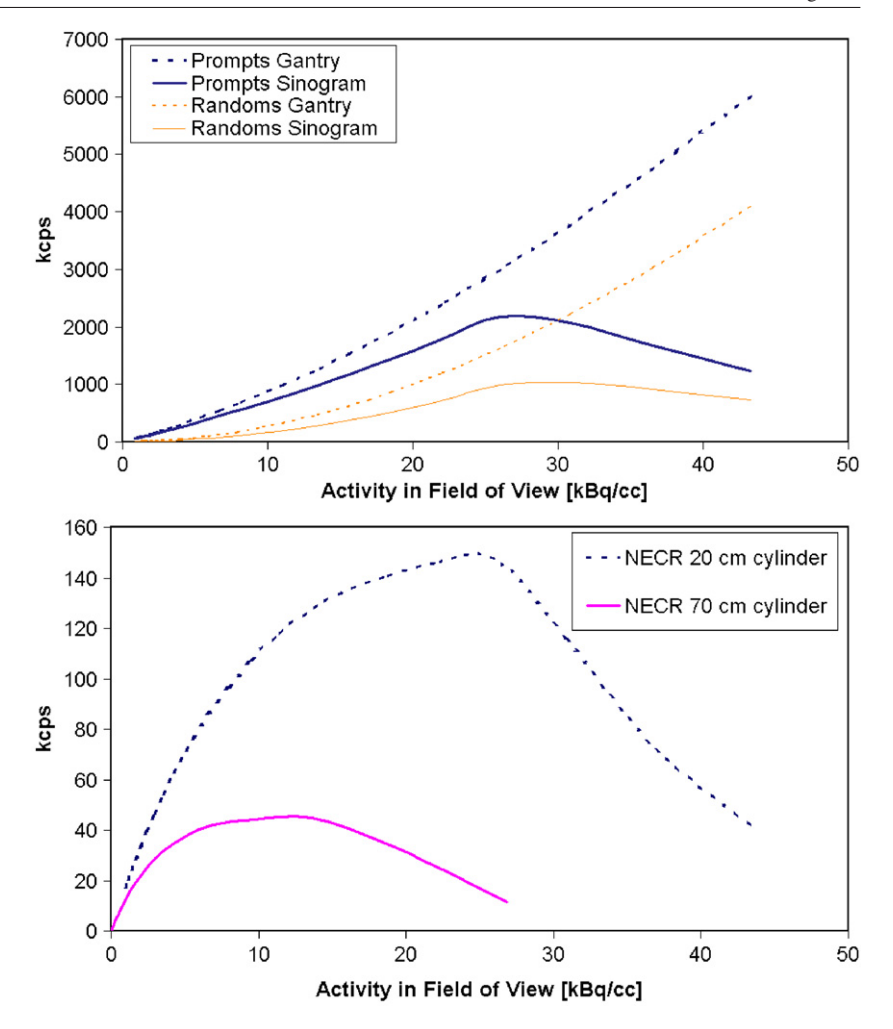
Figure 4. NEMA-1994 (top) and NEMA-2001 (bottom) count rates. Trues, corrected for dead time and decay are also included.

sensitivities as measured on the gantry, hence prior to sinogram binning (table 3). This number corresponds to the highest possible sensitivity achievable, by including all line of responses in the sinogram. The sensitivity slightly improves towards the edge of the axial FOV. This is probably due to the fact that photons emitted towards the edge of the FOV on average enter the crystal under a larger angle as compared to photons coming from the centre of the FOV. The larger angle results in a larger path through the crystal and, hence, a larger probability of interacting and being detected.

The NEMA-1994 volume sensitivity of the central 17 cm of the axial FOV is also included. This sensitivity is determined after corrections for randoms and scatter. Given the volume of the central 17 cm of the phantom (5340 ml), one could convert the volume sensitivity from cps kBq^{-1} ml^{-1} to cps Bq^{-1}. This results in an absolute sensitivity of approximately 0.5%, much lower than 2.5%, as found using NEMA-2001, which is mainly due to attenuation effects only found in the NEMA-1994 phantom.

Figure 5. Top: a comparison between prompts and random count rates as measured by the gantry (coincidence controller) and as measured in the sinograms. Bottom: NEC-2R numbers for the 20 cm (NEMA-1994) and 70 cm cylinders (NEMA-2001).

Table 3. NEMA-2001 absolute sensitivities for the two line-source positions and the NEMA-1994 volume sensitivity. The values in brackets are the sensitivities as measured on the gantry, hence without the loss of sinogram data compression.

Sensitivity (NEMA-2001)		Sensitivity (NEMA-1994)
Centre	10 cm off-centre	20 cm cylinder
2.5% (2.9%)	2.7% (3.1%)	31.0 cps kBq^{-1} ml^{-1}

5.4. Accuracy of corrections for count losses and randoms

The count rate measurements of section 5.2 were also used to assess the accuracy of corrections for count losses and randoms during reconstruction. In figure 7, the residual errors in the reconstructed central 17 cm of the axial FOV are shown for the 20 and 70 cm phantoms
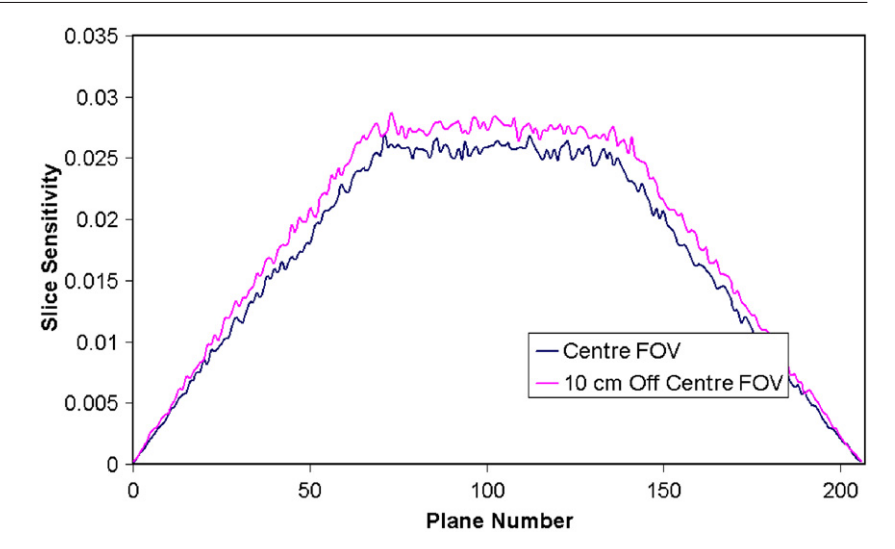
Figure 6. NEMA-2001 absolute sensitivity in percentage as function of plane number.

and for different reconstruction methods. The error is expressed as a percentage difference in reconstructed activity as compared to the reconstructed activity at 1 kBq cc^{-1}. At high activities, large errors are visible. As already noted in section 5.2, these deviations are due to count losses at the level of the acquisition computer. At lower activities the 2D FBP and 3D OP-OSEM with scatter correction reconstructions have a similar, but significant, error. This error cannot be seen in the 2D FBP reconstructions without scatter correction.
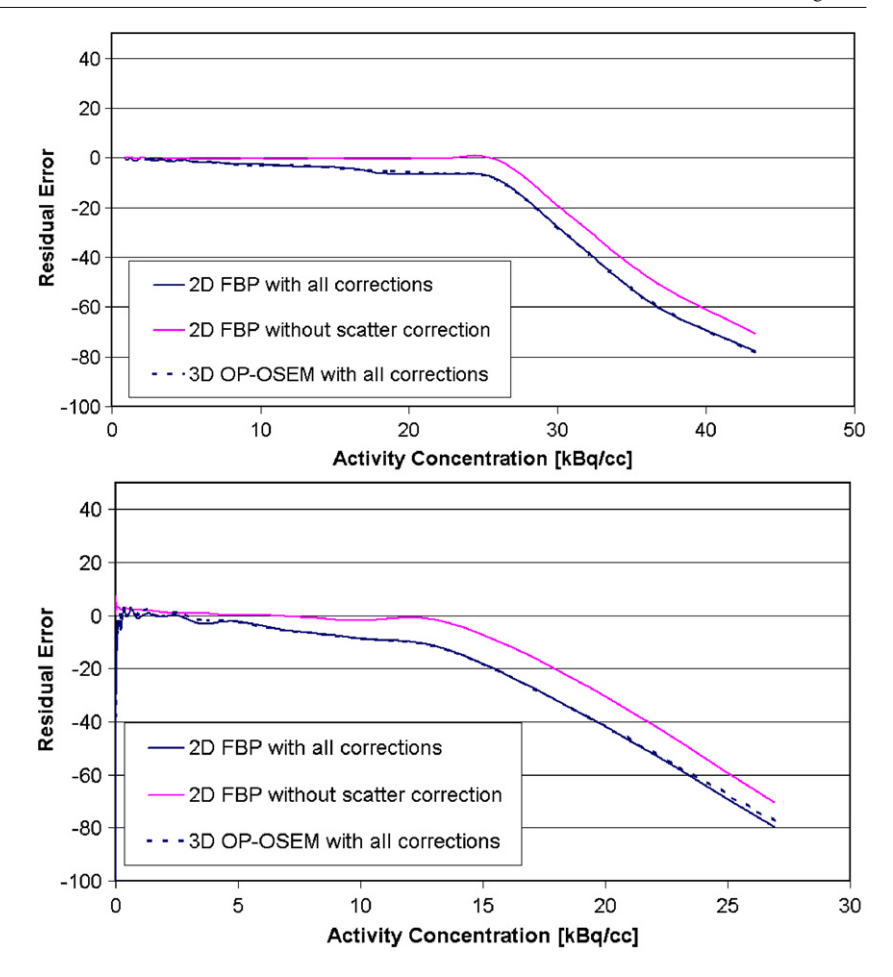
This finding is partly in agreement with scatter fraction results, as shown in figure 3. At the end of the scanner set-up process, the scatter correction algorithm needs to be tuned. During this process the algorithm, however, is optimized at a single activity or count rate instead for every situation anew. Another source of the underestimation might be out-of-the-FOV activity, suggested by the larger error in the NEMA-2001 phantom as compared to the NEMA-1994 phantom.

5.5. Uniformity, image quality, accuracy of attenuation and scatter corrections

Uniformity of the reconstructed images was assessed using the NEMA-1994 20 cm cylinder, homogeneously filled with activity. In every plane of the reconstructed image, a total of 33 square ROIs were drawn to get an average plane background value, plane non-uniformities and plane coefficients of variation between the ROI values. As can be seen from figure 8, the deviation from the volume mean varied between -6% and 8%, with larger deviations towards the back of the scanner (lower plane numbers). Maximum and minimum non-uniformities, as well as the coefficients of variation, are relatively constant throughout the axial FOV.

In a similar way, volume uniformity (between all ROIs in the volume) and system uniformity (between averages in slices) were calculated (table 4). These numbers are somewhat worse than those reported for the HR+ in a 3D mode, where the coefficient of variation equalled 5.0% and 1.7% for the volume and system uniformity, respectively (Brix *et al* 1997).

In order to assess the performance of the normalization and attenuation and scatter correction in the case of a non-homogeneous density distribution, the cylinder was equipped with water, air and Teflon inserts containing no activity. The acquired data were reconstructed using 3D OP-OSEM, including attenuation and scatter correction and normalization. The

Figure 7. Residual errors in reconstructed images of the NEMA-1994 20 cm cylinder (top) and the NEMA-2001 70 cm cylinder (bottom).

Table 4. Maximum and minimum volume and system uniformities and coefficients of variation according to the NEMA-1994 protocol.

	Maximum non-uniformity (%)	Minimum non-uniformity (%)	CV (%)
Volume uniformity	19.8	−18.9	6.3
System uniformity	8.3	−6.0	3.1

background per slice in the cylinder was determined by averaging nine ROIs. From these ROI values, the non-uniformity per slice was calculated. Since the reconstructed activity in the inserts is ideally zero, the ROI values can be normalized to these background values to obtain the relative errors. Figure 9 shows these numbers expressed as a percentage error. Whilst the water and air inserts show a uniform error over all planes, the Teflon insert has increasing deviation towards the back of the scanner. The values are comparable to the HR+, where reported errors varied between −20% (Teflon insert) and over 10% for the air insert.
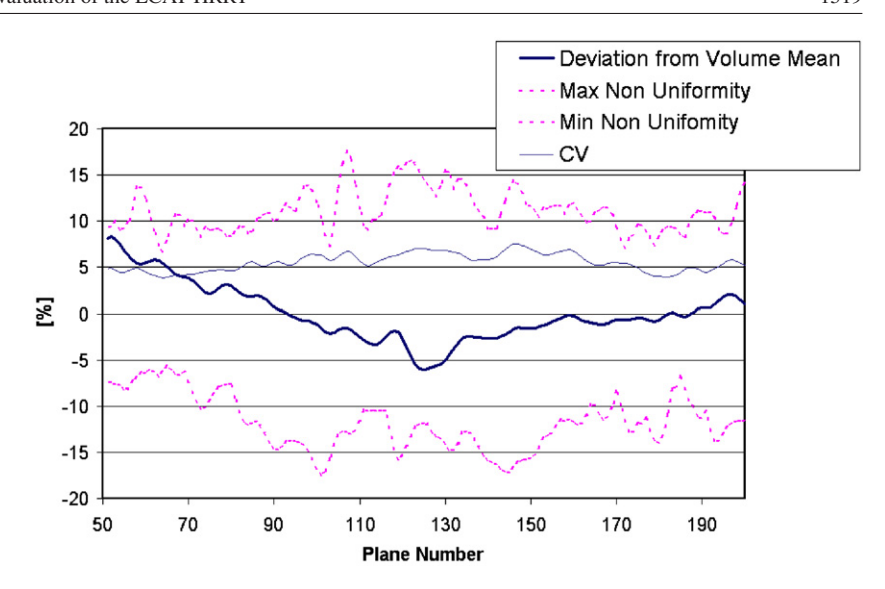
Figure 8. Values of non-uniformities (max, min and deviation from the volume mean) and coefficients of variation per plane.

Table 5. Hot CRC_{HOT} and cold sphere CRC_{COLD} contrast recovery coefficients for the two contrast ratios. Standard deviations were calculated using the four acquired images per ratio.
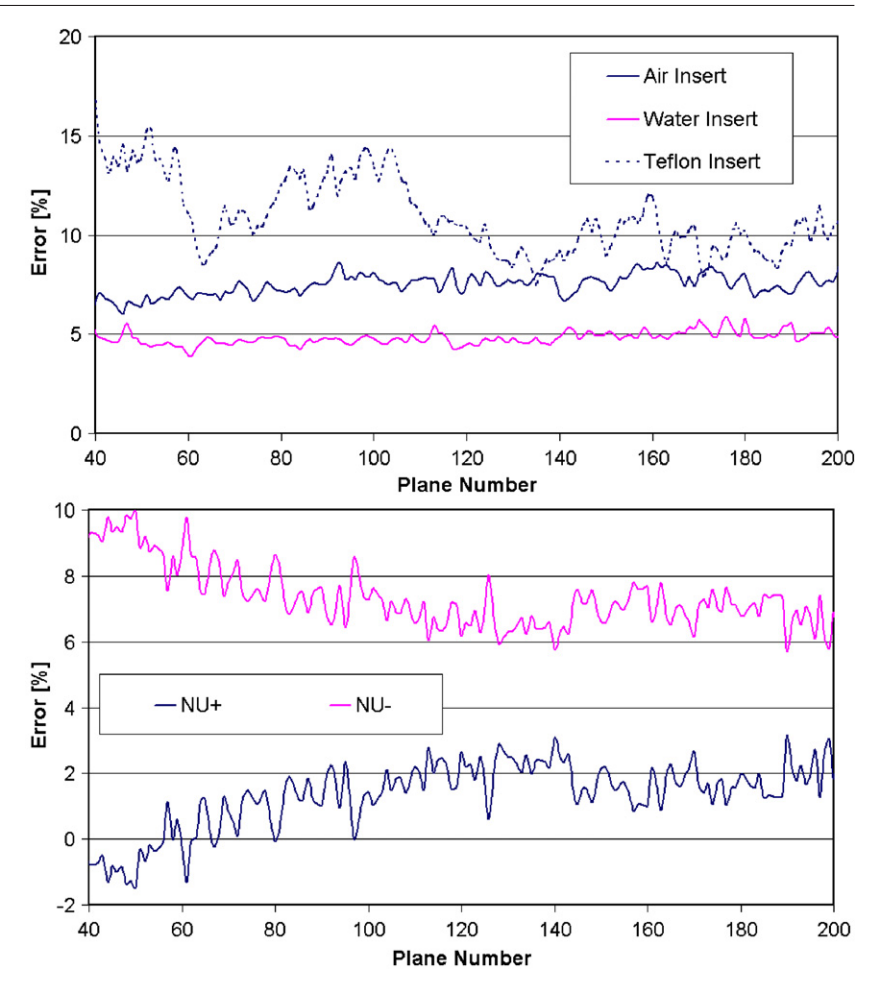
Sphere diameter (cm)	Contrast 8:1	Contrast 4:1
1.00 (CRC_{HOT})	0.58 ± 0.01	0.60 ± 0.06
1.25 (CRC_{HOT})	0.73 ± 0.01	0.69 ± 0.01
1.58 (CRC_{HOT})	0.81 ± 0.01	0.81 ± 0.02
2.22 (CRC_{HOT})	0.94 ± 0.01	0.94 ± 0.01
2.50 (CRC_{COLD})	0.81 ± 0.01	0.82 ± 0.01
3.14 (CRC_{COLD})	0.85 ± 0.00	0.84 ± 0.01

In figure 9, the non-uniformity of attenuation correction is also given for every plane, expressed as the largest and smallest deviation from the plane mean. Again, larger non-uniformities are seen at the back of the scanner.

For the image quality test, the 20 cm cylinder was equipped with hot and cold spheres. Data sets were acquired with sphere to background ratios of 8:1 and 4:1. For every ratio, four measurements of 15 min each were acquired. Reconstructions were performed using 3D OP-OSEM, including all corrections. Figure 10 shows a slice of the images through the smallest sphere, but not necessarily through the centre of the larger spheres. Hot sphere and cold sphere contrast recovery coefficients are given in table 5. Clearly, even the smallest sphere can be resolved without problem. For assessment of the brain image quality, a 3D OP-OSEM reconstruction of the Hoffman brain phantom (scan duration 1 h, activity 7 kBq cc^{-1} ^{18}F) is also included (figure 11). The horizontal steps in the coronal view are due to the physical slab thickness of the phantom.

5.6. Examples of human brain and small animal scans

Figure 12 shows an example of a whole body scan of a Whistar rat, injected with 37 MBq FDG. Since the rat can be imaged from top to toe in one bed position and the myocardium

Figure 9. Top: reconstructed values in the three inserts expressed as percentage of the plane background. Bottom: non-uniformity of attenuation correction for every plane. NU+ and NU− are the maximum and minimum ROI values in each slice compared to the slice average.
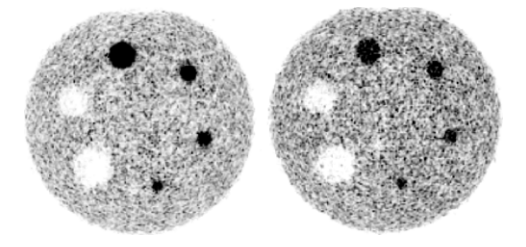

Figure 10. Cylinder sphere to background ratios of 8:1 (left) and 4:1 (right).

can easily be outlined, use of image-derived input functions should be possible. The total acquisition duration of the shown frame was 15 min.
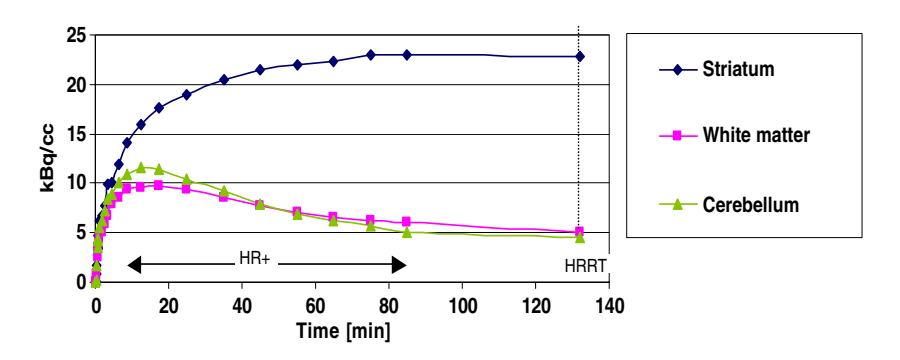
Evaluation of PET brain studies showed that ROI values of several regions in the HRRT [18F]-FP-ß-CIT images were within 8% of the values extrapolated from HR+ time-activity curves. An example of time-activity curves taken from the HR+ and HRRT data is given in

Figure 11. 3D OP-OSEM reconstructions of the Hoffman brain phantom. As a reference, the true activity distribution is also included (Data Spectrum Corporation, USA). Left: axial view, right: coronal view.

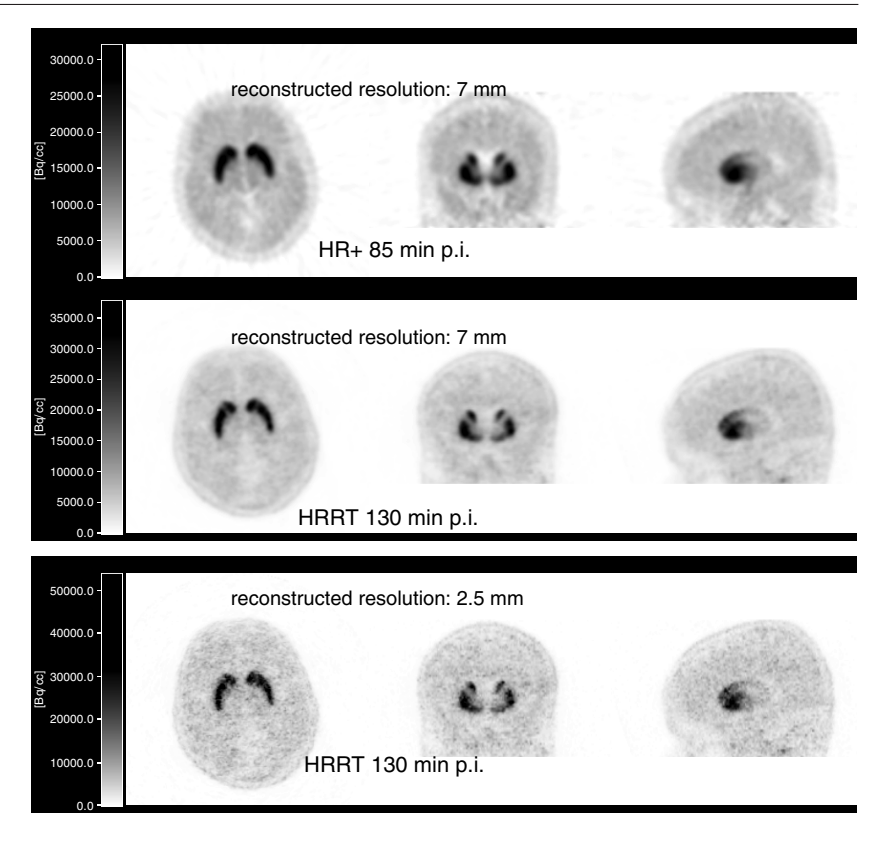**Figure 12.** 3D OP-OSEM reconstruction of an FDG injected rat.

Figure 13. Time-of-activity curves of various brain locations taken from the HR+ (first 23 frames) and HRRT images (last frame).

figure 13. Furthermore, visual inspection revealed that HRRT images were similar to HR+ images, but with superior resolution (figure 14).

6. Discussion

In this study, the commercial second generation HRRT PET scanner has been characterized by means of phantom experiments and a concise clinical evaluation. In order to ensure

Figure 14. Cross-sectional planes through an aligned HR+ frame and HRRT frames. For a comparison, the HRRT frames are shown at different reconstructed resolutions.

a complete description and to enable a direct comparison with other scanners, the NEMA protocol was taken as a guideline. Although recently NEMA NU-2 2001 replaced the NEMA NU-2 1994 protocol, some parts of the latter were still included in this study, as it partially contains experiments that are more appropriate for a brain scanner (National Manufacturers Association 1994). The NEMA NU-2 2001 is more directed towards PET scanners that are primarily used for whole body oncology studies. Hence, the NEMA-1994 homogeneous cylinder was used for the measurement of the hot and cold sphere recovery, as its size is similar to the human head. In contrast, the NEMA-2001 phantom used for the recovery measurement is thorax-shaped and includes a compartment resembling a lung, a situation less relevant for a brain scanner.

An advantage of including both protocols is that a comparison can yield extra information, such as the effect of out-of-FOV activity; the NEMA-1994 count rate test is performed using a 19 cm long cylinder, hence falling completely within the large FOV of the HRRT, and results in a peak NEC rate of 148 kcps. The NEMA-2001 prescribes a 70 cm cylinder, resembling a more realistic situation where an activity is also located outside the FOV. The increased randoms rate degrades the peak NEC rate to 45 kcps. This difference, however, is much smaller than that found in whole body PET scanners, such as the GE Advance 3D BGO scanner where the peak NEC rate drops from 146 kcps (NEMA-1994) to 19.2 for the NEMA-2001 phantom (Daube-Witherspoon *et al* 2002). Although the shorter coincidence time window for the HRRT (6 ns instead of 12 ns for BGO) and corresponding lower random rates play an important role as

pointed out by Eriksson *et al* (2002), also important are the smaller gantry opening and the tungsten shielding that make the scanner less sensitive to activity out of the FOV. This effect of shielding is corroborated by the scatter fractions that go from 41.6% (NEMA-1994) to 45.2% (NEMA-2001), a decline again much smaller as compared with numbers for the GE Advance (34.7% to 47.1%) (Daube-Witherspoon *et al* 2002).

Although the HRRT is in many ways technically superior to predecessors such as the HR+ BGO scanner, its high sensitivity, large FOV and high resolution and the default acquisition in the list mode, demand powerful data processing systems that verge on or are beyond current computer standards (Vollmar *et al* 2002). As an example, the NEMA-2001 count rate study with 370 MBq (a clinical relevant dose) in the 70 cm phantom generates in 1 h a list mode file of approximately 100 Gbyte in size. This not only demands large data storage discs and backup facilities, but also requires very fast data handling from the PET acquisition computer, considering the rate at which the data stream comes in. Figure 7 shows that when more than 150 MBq is present in the FOV (NEMA-1994) or 250 MBq in the 70 cm phantom, activity is already grossly underestimated. This is most likely due to a data rate exceeding the processing speed of the PET acquisition computer, based on the comparison between the count rate as measured in the gantry and as found in the final acquired sinograms (figure 5). While the latter shows large dead time effects with 150 MBq in the FOV, the gantry count rate seems unaffected. Altogether, acquisitions such as blood flow studies using 15-O water, where injected dosages normally exceed 1 GBq, will certainly put the system to the test. The high sensitivity of the HRRT, however, possibly allows for the use of lower dose levels.

As already mentioned, the typical size of the acquired data files is considerable. The tens of Gbytes of the list mode data produced during a typical patient scan have to be converted to a series of dynamic prompts and randoms sinograms, 80 Gbyte in size for 40 frames in span 3, originally the default sinogram size. Although an HRRT installation typically includes a 16 CPU reconstruction cluster, the 3D OP-OSEM reconstruction of such a large sinogram including all corrections currently still takes about 1 h (per frame), which explains the choice for this latter sinogram size (Jones *et al* 2003). A reasonable alternative to 3D OP-OSEM would be the use of a 3D FBP algorithm, which hypothetically can resolve the axial resolution and is not hampered by biases due to sparse sinograms (Baghaei *et al* 2004, Herzog *et al* 2004). Its less beneficial noise properties may not be so important for reconstructions of dynamic scans, as quantification rather than image quality is the main aim for these studies.

While the volume and system non-uniformities were comparable to values for the ECAT HR+ (Brix *et al* 1997), the slice uniformities show a significant decline towards the back of the scanner (lower plane numbers in figures 8 and 9). The relatively large deviation can be attributed to differences in reconstructed counts per slice. Although this could be due to normalization errors, earlier published results (De Jong *et al* 2005a), revealed that this inter-plane uniformity significantly improves when no scatter correction is performed. Despite the fact that great care was taken in manually fine tuning the algorithm, it also showed underestimation in the *'accuracy of corrections for count losses and randoms'* (figure 7), where omission of the scatter correction resulted in improved linearity. Part of this, however, can be attributed to the fact that the correction algorithm does not incorporate the count rate-dependent scatter fraction. Nevertheless, the hot and cold sphere test did show high accuracy in the recovery of activity, and in the clinical evaluation the HRRT images gave quantitative information that only deviated a few per cent from the HR+ data (after resolution matching of both data sets and extrapolation of the HR+ data). None of these analysed regions, however, were located near the back of the scanner.

Developments are also to be expected in the scanner set-up procedure. At this time, manual fine tuning is still required, even though an automated adjustment of the scanner is

supported. As was illustrated by a recent multi-centre comparison (Sossi *et al* 2005), this promotes operator-dependent performance. It has to be mentioned here that no prior multi-centre scanner performance study has been published before, so it is unclear how the results of this comparison relate to other scanners.

Compared to dedicated small animal PET scanners such as the microPET P4 (Primate 4-ring from Concorde Microsystems Inc, Knoxville, TN, performance data from Tai *et al* (2001)) with a higher resolution (2.3 mm versus 1.75 mm), the HRRT has the benefit of a higher (point source) sensitivity (approximately 6% versus 2.25%) and a much larger axial (25 cm versus 7.8 cm) and transaxial FOV (31 cm versus 19 cm), enabling the study of a multitude of rats or mice from head to tail. The large FOV furthermore ensures that the whole brain, including the brain stem, is imaged in one bed position. After two prototypes, the scanner has been fully developed when it comes to gantry hardware. Ongoing improvements to the software and data processing and correction algorithms will lead to a scanner that can set the standard in PET brain research.

Acknowledgments

References

Baghaei H, Wong W H, Uribe J, Li H D, Wang Y, Liu Y Q, Xing T, Ramirez R, Xie S P and Kim S 2004 A comparison of four-image reconstruction algorithms for 3-d PET imaging of MDAPET camera using phantom data *IEEE Trans. Nucl. Sci.* **51** 2563–9

Bailey D L, Jones T and Spinks T J 1991 A method for measuring the absolute sensitivity of positron emission tomographic scanners *Eur. J. Nucl. Med.* **18** 374–9

Bartzakos P and Thompson C J 1991 A pet detector with depth-of-interaction determination *Phys. Med. Biol.* **36** 735–48

Beekman F J, van der Have F, Vastenhouw B, van der Linden A J A, van Rijk P P, Burbach J P and Smidt M P 2005 U-SPECT-I: a novel system for submillimeter-resolution tomography with radiolabeled molecules in mice *J. Nucl. Med.* **46** 1194–200

Boellaard R, Buijs F, De Jong H W A M, Lenox M, Gremillion T and Lammertsma A A 2003a Characterization of a single LSO crystal layer high resolution research tomograph *Phys. Med. Biol.* **48** 429–48

Boellaard R, De Jong H W A M, Molthoff C F M, Buijs F, Lenox M, Nutt R and Lammertsma A A 2003b Use of an in-field-of-view shield to improve count rate performance of the single crystal layer high-resolution research tomograph PET scanner for small animal brain scans *Phys. Med. Biol.* **48** N335–42

Brambilla M, Secco C, Dominietto M, Matheoud R, Sacchetti G and Inglese E 2005 Performance characteristics obtained for a new 3-dimensional lutetium oxylorthosilicate-based whole-body PET/CT scanner with the national electrical manufacturers association NU 2-2001 standard *J. Nucl. Med.* **46** 2083–91

Brix G, Zaers J, Adam L E, Bellemann M E, Ostertag H, Trojan H, Haberkorn U, Doll J, Oberdorfer F and Lorenz W J 1997 Performance evaluation of a whole-body PET scanner using the NEMA protocol *J. Nucl. Med.* **38** 1614–23

Casey M E, Eriksson L, Schmand M, Andreaco M S, Paulus M, Dahlbom M and Nutt R 1997 Investigation of LSO crystals for high spatial resolution positron emission tomography *IEEE Trans. Nucl. Sci.* **44** 1109–13

Chatziioannou A F, Cherry S R, Shao Y P, Silverman R W, Meadors K, Farquhar T H, Pedarsani M and Phelps M E 1999 Performance evaluation of microPET: a high-resolution lutetium oxyorthosilicate PET scanner for animal imaging *J. Nucl. Med.* **40** 1164–75

Cherry S R *et al* 1997 MicroPET: a high resolution PET scanner for imaging small animals *IEEE Trans. Nucl. Sci.* **44** 1161–6

Comtat C, Bataille F, Michel C, Jones J P, Sibomana M, Janeiro L and Trébossen R 2004 OSEM-3D reconstruction strategies for the ECAT HRRT *Conf. Rec. of the 2004 IEEE Nucl. Sci. Symp. and Med. Imaging Conf. (Rome 2004)*

Daube-Witherspoon M E *et al* 2002 PET performance measurements using the NEMA NU 2-2001 standard *J. Nucl. Med.* **43** 1398–409

De Jong H W A M, Boellaard R, Knoess C, Lenox M, Michel C, Casey M and Lammertsma A A 2003 Correction methods for missing data in sinograms of the HRRT PET scanner *IEEE Trans. Nucl. Sci.* **50** 1452–6

De Jong H W A M, Boellaard R, Lenox M, Michel C and Lammertsma A A 2004 Correction for emission contamination in transmission scans for the high resolution research tomograph *IEEE Trans. Nucl. Sci.* **51** 673–6

De Jong H W A M, Boellaard R, van Berckel B N M, Ponssen M and Lammertsma A A 2005a Quantitative accuracy of the high resolution research tomograph: experimental and clinical evaluation *Conf. Rec. of the 2005 Brain and BrainPET Meeting (Amsterdam 2005)*

De Jong H W A M, Perk L, Visser G W M, Boellaard R, van Dongen G A M S and Lammertsma A A 2005b High resolution ET imaging characteristics of 68-Ga, 124-I and 89-Zr compared to 18-F *Conf. Rec. of the 2005 IEEE Nucl. Sci. Symp. and Med. Imaging Conf. (Puerto Rico 2005)*

Defrise M, Kinahan P E, Townsend D W, Michel C, Sibomana M and Newport D F 1997 Exact and approximate rebinning algorithms for 3-D PET data *IEEE Trans. Med. Imag.* **16** 145–58

Eriksson L *et al* 2002 The ECAT HRRT: NEMA Nec evaluation of the HRRT system, the new high-resolution research tomograph *IEEE Trans. Nucl. Sci.* **49** 2085–8

Eriksson L *et al* 2005 The ECAT HRRT: an example of NEMA scatter estimation issues for LSO-based PET systems *IEEE Trans. Nucl. Sci.* **52** 90–4

Heiss W D, Habedank B, Klein J C, Herholz K, Wienhard K, Lenox M and Nutt R 2004 Metabolic rates in small brain nuclei determined by high-resolution PET *J. Nucl. Med.* **45** 1811–5

Herzog H, Tellmann L, Hocke C, Pietrzyk U, Casey M E and Kuwert T 2004 NEMA NU2–2001 guided performance evaluation of four siemens ECAT PET scanners *IEEE Trans. Nucl. Sci.* **51** 2662–9

Huber J S, Moses W W, Jones W F and Watson C C 2002 Effect of Lu-176 background on singles transmission for LSO-based PET cameras *Phys. Med. Biol.* **47** 3535–41

Jones J P, Jones W F, Kehren F, Burbar Z, Reed J H, Lenox M W, Baker K, Byars L G, Michel C and Casey M E 2003 Clinical time OSEM3D: infrastructure issues *Conf. Rec. of the 2003 IEEE Nucl. Sci. Symp. and Med. Imaging Conf. (Portland 2003)*

Lammertsma A A 2001 PET/SPECT: functional imaging beyond flow *Vis. Res.* **41** 1277–81

Lammertsma A A, Hume S P, Myers R, Ashworth S, Bloomfield P M, Rajeswaran S, Spinks T and Jones T 1995 Pet scanners for small animals *J. Nucl. Med.* **36** 2391–2

Matej S, Karp J S, Lewitt R M and Becher A J 1998 Performance of the Fourier rebinning algorithm for PET with large acceptance angles *Phys. Med. Biol.* **43** 787–95

National Manufacturers Association 1994 *NEMA Standards Publication NU 2-1994* (Washington, DC: National Electrical Manufacturers Association)

National Manufacturers Association 2001 *NEMA Standards Publication NU 2-2001* (Washington, DC: National Electrical Manufacturers Association)

Nuyts J, Michel C and Dupont P 2001 Maximum-likelihood expectation-maximization reconstruction of sinograms with arbitrary noise distribution using NEC-transformations *IEEE Trans. Med. Imag.* **20** 365–75

Pomper M G and Lee J S 2005 Small animal imaging in drug development *Curr. Pharm. Des.* **11** 3247–72

Schmand M, Eriksson L, Casey M E, Andreaco M S, Melcher C, Wienhard K, Flugge G and Nutt R 1998 Performance results of a new DOI detector block for a high resolution PET-LSO research tomograph HRRT *IEEE Trans. Nucl. Sci.* **45** 3000–6

Schramm N U, Ebel G, Engeland U, Schurrat T, Behe M and Behr T M 2003 High-resolution SPECT using multipinhole collimation *IEEE Trans. Nucl. Sci.* **50** 315–20

Seidel J, Vaquero J J and Green M V 2003 Resolution uniformity and sensitivity of the NIH ATLAS small animal PET scanner: comparison to simulated LSO scanners without depth-of-interaction capability *IEEE Trans. Nucl. Sci.* **50** 1347–50

Sossi V *et al* 2005 The second generation HRRT—a multi centre scanner performance investigation *Conf. Rec. of the 2005 IEEE Nucl. Sci. Symp. and Med. Imaging Conf. (Puerto Rico 2005)*

Tai Y C, Chatziioannou A, Siegel S, Young J, Newport D, Goble R N, Nutt R E and Cherry S R 2001 Performance evaluation of the microPET P4: a PET system dedicated to animal imaging *Phys. Med. Biol.* **46** 1845–62

Tsuda T, Murayama H, Kitamura K, Inadama N, Yamaya T, Yoshida E, Nishikido F, Hamamoto M, Kawai H and Ono Y 2006 Performance evaluation of a subset of a four-layer LSO detector for a small animal DOI PET scanner: jPET-RD *IEEE Trans. Nucl. Sci.* **53** 35–9

Vaska P and Alexoff D L 2003 Effects of natural LSO radioactivity on microPET quantitation *J. Nucl. Med.* **44** 138P

Vollmar S, Michel C, Treffert J T, Newport D F, Casey M, Knoss C, Wienhard K, Liu X, Defrise M and Heiss W-D 2002 HeinzelCluster: accelerated reconstruction for FORE and OSEM3D *Phys. Med. Biol.* **47** 2651–8

Wang J L and Maurer L 2005 Positron emission tomography: applications in drug discovery and drug development *Curr. Top. Med. Chem.* **5** 1053–75

Watson C C 2000 New, faster, image-based scatter correction for 3D PET *IEEE Trans. Nucl. Sci.* **47** 1587–94

Watson C C, Casey M E, Eriksson L, Mulnix T, Adams D and Bendriem B 2004 NEMA NU 2 performance tests for scanners with intrinsic radioactivity *J. Nucl. Med.* **45** 822–6

Weber S *et al* 1999 Evaluation of the TierPET system *IEEE Trans. Nucl. Sci.* **46** 1177–83

Wienhard K *et al* 2002 The ECAT HRRT: performance and first clinical application of the new high resolution research tomograph *IEEE Trans. Nucl. Sci.* **49** 104–10

Wong W H, Uribe J, Hicks K and Hu G J 1995 An analog decoding Bgo block detector using circular photomultipliers *IEEE Trans. Nucl. Sci.* **42** 1095–101